nature nanotechnology

Article

https://doi.org/10.1038/s41565-024-01626-0

Complete miscibility of immiscible elements at the nanometre scale

Received: 17 January 2023

Accepted: 2 February 2024

Published online: 01 March 2024

Check for updates

Peng-Cheng Chen[1,2,6,7], Mengyu Gao[3,7], Caitlin A. McCandler[1,3,7], Chengyu Song[4], Jianbo Jin[2], Yao Yang[2,5], Arifin Luthfi Maulana[3], Kristin A. Persson[1,3,4] & Peidong Yang[1,2,3]

Understanding the mixing behaviour of elements in a multielement material is important to control its structure and property. When the size of a multielement material is decreased to the nanoscale, the miscibility of elements in the nanomaterial often changes from its bulk counterpart. However, there is a lack of comprehensive and quantitative experimental insight into this process. Here we explored how the miscibility of Au and Rh evolves in nanoparticles of sizes varying from 4 to 1 nm and composition changing from 15% Au to 85% Au. We found that the two immiscible elements exhibit a phase-separation-to-alloy transition in nanoparticles with decreased size and become completely miscible in sub-2 nm particles across the entire compositional range. Quantitative electron microscopy analysis and theoretical calculations were used to show that the observed immiscibility-to-miscibility transition is dictated by particle size, composition and possible surface adsorbates present under the synthesis conditions.

Multielement materials are of particular interest in catalysis[1,2], structural materials[3–5], optoelectronic devices[6,7], thermal energy harvesting[8,9] and quantum computing[10]. The chemical, mechanical and electronic interplay between multiple elements in a material, either in an alloyed or phase-separated format, allows the material to harness multielement synergy to achieve enhanced properties. Controlling the alloying and phase separation behaviour of elements, usually guided by the bulk phase diagrams[11], is a prerequisite to realize those target properties. Compared with the bulk scale, miniaturizing the dimensions of multielement materials to the nanoscale can often substantially change their physical and chemical properties. In particular, novel multielement nanomaterials have been systematically created[12–21] and new properties have been identified for a variety of applications[1,2,6,7,10,22–25].

At the same time, researchers have noticed that the bulk phase diagram may not apply at the nanoscale. For example, theoretical simulations on nanoparticles composed of immiscible elements have unveiled the shrinking of the miscibility gap in the size regime of 1–10 nm (refs. 26–29). Furthermore, mixing of immiscible elements such as Ag–Ni, Ag–Cu, Au–Rh and Au–Pt have been experimentally observed in nanomaterials made by colloidal co-reduction synthesis[13,30–35], physical co-sputtering[36] or quenching of a liquid or gas elemental mixture prepared at a high temperature[22,37,38]. However, it is unclear whether these mixed nanostructures are thermodynamic alloys or kinetically trapped structures. Besides, it remains difficult to synthesize ultrasmall nanoparticles at a thermodynamic state spanning a broad compositional range. To date, there is a lack of comprehensive experimental insight into how material dimensions affect their thermodynamic phase separation behaviour and how this deviates from the bulk phase diagram. At the small length scales of nanomaterials and atomic clusters, the large proportion of surface atoms is a crucial factor in controlling the material's thermodynamic state[37–41]. In particular, atoms on terraces, edges and corners possess fewer neighbouring atoms than atoms in the bulk, resulting in a decreased coordination number between immiscible elements and therefore a decreased enthalpy of mixing of the system. In addition, defects and structural relaxation in nanoparticles can relieve strain caused by the lattice and size mismatch of different

[1]Kavli Energy Nanoscience Institute, University of California, Berkeley, CA, USA. [2]Department of Chemistry, University of California, Berkeley, CA, USA. [3]Department of Materials Science and Engineering, University of California, Berkeley, CA, USA. [4]Molecular Foundry, Lawrence Berkeley National Laboratory, Berkeley, CA, USA. [5]Miller Institute, University of California, Berkeley, CA, USA. [6]Present address: Department of Materials Science, Fudan University, Shanghai, China. [7]These authors contributed equally: Peng-Cheng Chen, Mengyu Gao, Caitlin A. McCandler. e-mail: p_yang@berkeley.edu

https://doi.org/10.1038/s41565-024-01626-0

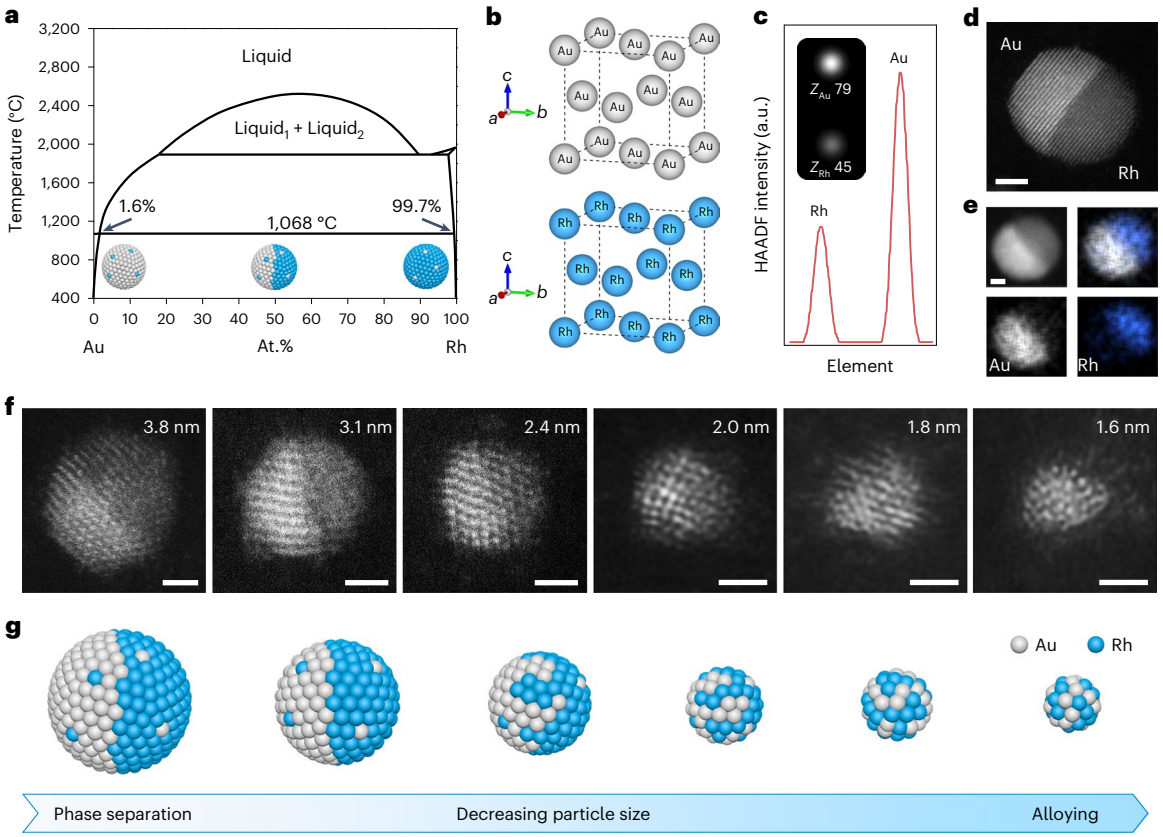

Fig. 1 | Overview of the size-dependent miscibility relationship between Au and Rh. a, Bulk phase diagram of the Au–Rh binary system[11]. **b**, Crystal structure of Au metal and Rh metal. The grey and blue atoms represent Au and Rh, respectively. **c**, Simulated HAADF-STEM intensity profile of single Au and Rh atoms. The inset shows the simulated HAADF-STEM image of single Au and Rh atoms. **d**,**e**, HAADF-STEM images (**d**) and EDS elemental mapping (**e**) of Au–Rh nanoparticles with sizes larger than 4 nm. Scale bars, 2 nm. **f**, HAADF-STEM images of Au–Rh nanoparticles of size decreased from 4 to 1 nm. Scale bars, 1 nm. **g**, Schematic of the transition from phase separation to alloying in 4–1 nm Au–Rh nanoparticles.

elements[27,42,43], further influencing the thermodynamic state. In a previous experimental study, we have shown that the solubility between Au and Rh increases to approximately 10% in particles of size between 4 and 12 nm, as opposed to the <1% solubility at the bulk scale[44]. Given the important role of surface atoms in influencing the thermodynamic state of the materials[40,41], it is possible that by further decreasing the particle size, even immiscible elements may fully mix.

Here, to examine whether this immiscibility-to-miscibility transition occurs, we investigate the thermodynamic phase separation behaviour of two immiscible elements (Au and Rh) in a nanoparticle with compositions varying from 15% Au to 85% Au and size between 4 and 1 nm. We show that unlike the bulk phase diagram, the phase separation behaviour of Au and Rh in a nanoparticle highly depends on the particle composition, size and surface passivation. The miscibility gap between Au and Rh can be eliminated spanning the whole compositional range in the sub-2 nm size regime. First-principles calculations show that different surface adsorbates, present under synthesis conditions, can sufficiently change the surface energies of Au and Rh to cause a cross-over in the thermodynamic phase stability.

Effect of particle size and composition on the phase separation behaviour

We chose Au and Rh as a model system because the two elements will segregate into two phases that are almost unary at temperature of <1,000 °C (Fig. 1a)[11]. Both virtually pure phases adopt a face-centred cubic lattice structure (Fig. 1b), which simplifies the structural analysis of the binary system. The two elements are not air sensitive, minimizing the influence of air-induced oxidation when characterizing the nanoparticles. In addition, Au and Rh have a large difference in atomic number, making them distinguishable by high-angle annular dark-field scanning transmission electron microscopy (HAADF-STEM) since the HAADF-STEM image intensity is proportional to the atomic number[45] ($I \propto Z^{1.7}$; Fig. 1c). To synthesize Au–Rh nanoparticles with the desired size and composition, polymer micelles made of polystyrene-*b*-poly (2-vinylpyridine) with metal salt precursors coordinated to the pyridyl groups were used as nanoreactors to mediate the nanoparticle synthesis. The micelles were spin coated on transmission electron microscopy (TEM) grids with carbon support films. The grids were thermally annealed under flowing Ar/H_2 to decompose the polymer template, convert metal precursors into nanoparticles and ensure that Au and Rh reach thermodynamic equilibrium (Supplementary Fig. 1).

The synthesized nanoparticles were characterized by aberration-corrected HAADF-STEM to assess the distribution of Au and Rh atoms and measured by energy-dispersive X-ray spectroscopy (EDS) to determine the composition. Au and Rh phase separate into two domains in nanoparticles larger than 4 nm, as verified by the elemental mapping and the contrast of Au and Rh domains in the HAADF-STEM images (Fig. 1d,e and Supplementary Fig. 2). To evaluate whether Au and Rh can be completely alloyed in a smaller-size particle, we first explored $Au_{0.5}Rh_{0.5}$ with diameters specifically tailored between 4 and 1 nm (Fig. 1f). When the particle size is larger than 3 nm, the contrast between Au and Rh domains indicates that Au–Rh adopts a heterodimer structure. When the particle size is decreased into the range of 2.2–1.8 nm, the interface between Au and Rh domains become more diffusive. The interface eventually disappears in every particle of size less than 1.8 nm. We also performed simulation on the HAADF-STEM images of around

https://doi.org/10.1038/s41565-024-01626-0

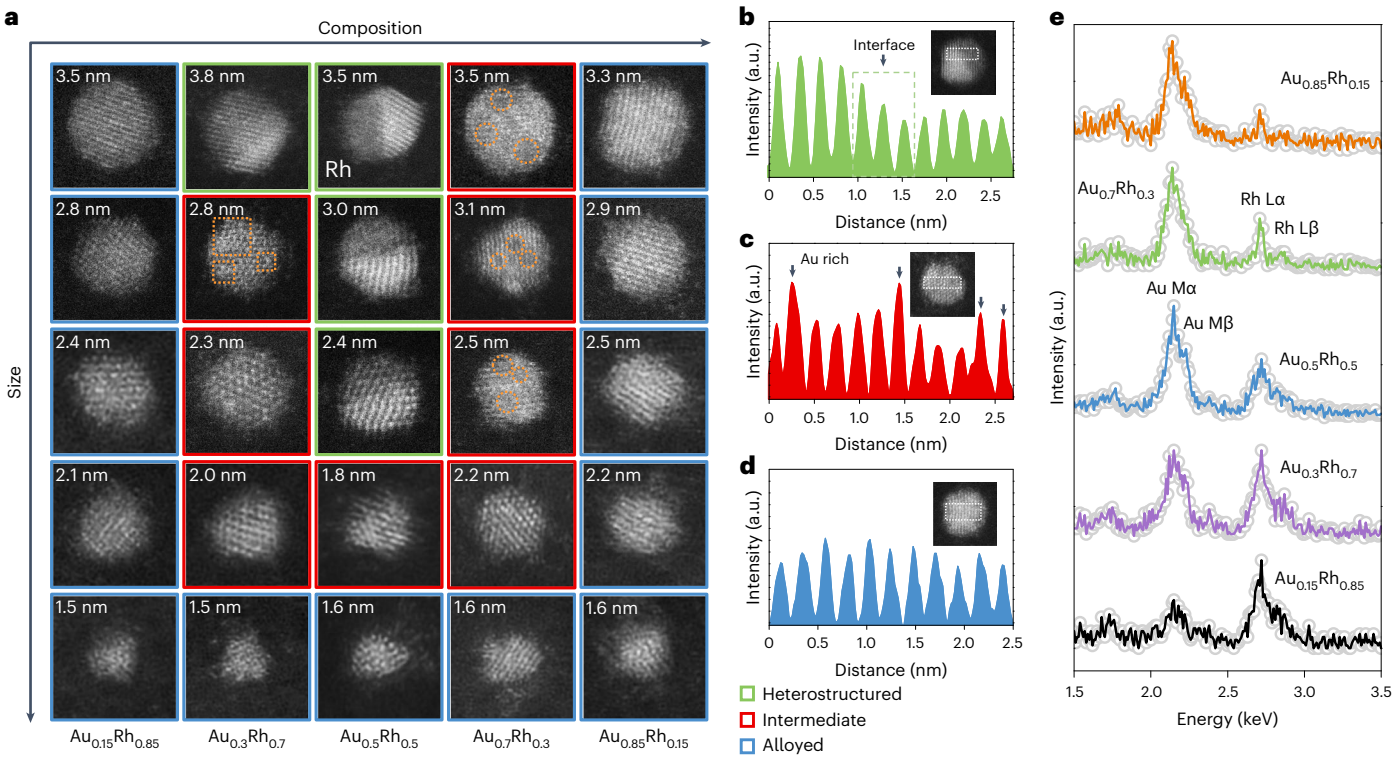

Fig. 2 | Closing the miscibility gap between Au and Rh at the nano- and cluster length scales. a, HAADF-STEM images of Au–Rh nanoparticles with composition changing from 15% Au to 85% Au (atomic ratio) and sizes between 4 and 1 nm. The orange squares highlight the Au domains split in the nanoparticles. The orange circles highlight the Rh domains split in the nanoparticles. **b**–**d**, Linescan profiles extracted from the HAADF-STEM images of Au–Rh nanoparticles possessing different Au–Rh mixing states, that is, heterostructured (**b**), intermediate (**c**) and alloyed (**d**). The insets show the HAADF-STEM images of the nanoparticles. The linescan curves are plotted based on the region highlighted by the white rectangular lines (Supplementary Fig. 11 provides details). **e**, EDS spectra of the five types of Au–Rh nanoparticle with different compositions.

1.6 nm Au–Rh particles with dimeric or core–shell structures. These structural features can be clearly identified by HAADF-STEM (Supplementary Figs. 3–6), but have never been experimentally observed. As such, the HAADF-STEM characterization suggests that Au–Rh nanoparticles undergo a transition from phase separation to alloy when the particle size is decreased from 4 to 1 nm (Fig. 1g).

To further understand the size effect, we systematically synthesized and investigated Au–Rh nanoparticles with five different compositions in the size regime of 4–1 nm (Fig. 2). The average compositions of the five types of nanoparticle are $Au_{0.15}Rh_{0.85}$, $Au_{0.3}Rh_{0.7}$, $Au_{0.5}Rh_{0.5}$, $Au_{0.7}Rh_{0.3}$ and $Au_{0.85}Rh_{0.15}$ (Fig. 2e and Supplementary Figs. 7–9). For this set of five samples, the mixing behaviour of Au and Rh is highly dependent on both particle composition and size. When the particle composition is in the range of 30–70% Au (Fig. 2a, second to fourth column), the particles generally exhibit a transition from heterostructured to intermediate and alloyed when the particle size changes from 4 to 1 nm. Specifically, nanoparticles of around 4 nm display a heterostructured state, where a sharp interface between Au and Rh can be clearly observed (Fig. 2a, green squares). By contrast, nanoparticles of 1.6 nm exhibit an alloyed structure, as evidenced by the disappearance of the interfaces and the even contrast in the scanning transmission electron microscopy (STEM) images (Fig. 2a, blue squares). In the size regime between the heterostructured and alloyed states, the nanoparticles manifest an intermediate structure in which Au or Rh forms multiple domains in a single nanoparticle and the phase boundaries are less sharp (Fig. 2a, red squares). Compared with these nanoparticles, no size-dependent transition is observed in nanoparticles composed of 15% Au or 85% Au. For these two specific compositions, Au and Rh can be alloyed in the entire 4–1 nm range (Fig. 2a, first and fifth columns). Together, both particle composition and size affect the separation state between Au and Rh, and a smaller particle size generally favours their mixing (Fig. 2a and Supplementary Fig. 10).

The three different mixing states between Au and Rh (heterostructured, intermediate and alloyed) are also confirmed by performing linescan analyses on the atomic-resolution STEM images. The linescan profile across the interface of a heterostructured particle reveals the separation between bright atomic columns and dark atomic columns, which can be assigned to the single Au domain and Rh domain in the nanoparticle (Fig. 2b and Supplementary Fig. 11). A sharp interfacial region within about three atomic columns can be found in the nanoparticle. For an intermediate nanoparticle (Fig. 2c), the bright atomic columns indicative of Au-rich columns are randomly distributed in the linescan profile, suggesting the formation of multiple Au or Rh domains in the particle due to the increased mixing level between Au and Rh. In the linescan profile of an alloyed nanoparticle (Fig. 2d), the intensity of all the atomic columns is relatively uniform, suggesting the well-mixed state between Au and Rh. In comparison with the three distinct states in Au–Rh nanoparticles, we also characterized pure Au and Rh nanoparticles in the size range of 4–1 nm (Supplementary Fig. 12). Their HAADF-STEM images exhibit homogeneous contrast, confirming that the observation of phase-separation-to-alloy transition is not an artefact caused by HAADF-STEM characterization.

Quantitative evaluation of the phase-separation-to-alloy transition

To further understand the transition, we quantitatively assessed the mixing state between Au and Rh by analysing the number and cross-sectional area of the minor element's domains in a nanoparticle,

https://doi.org/10.1038/s41565-024-01626-0

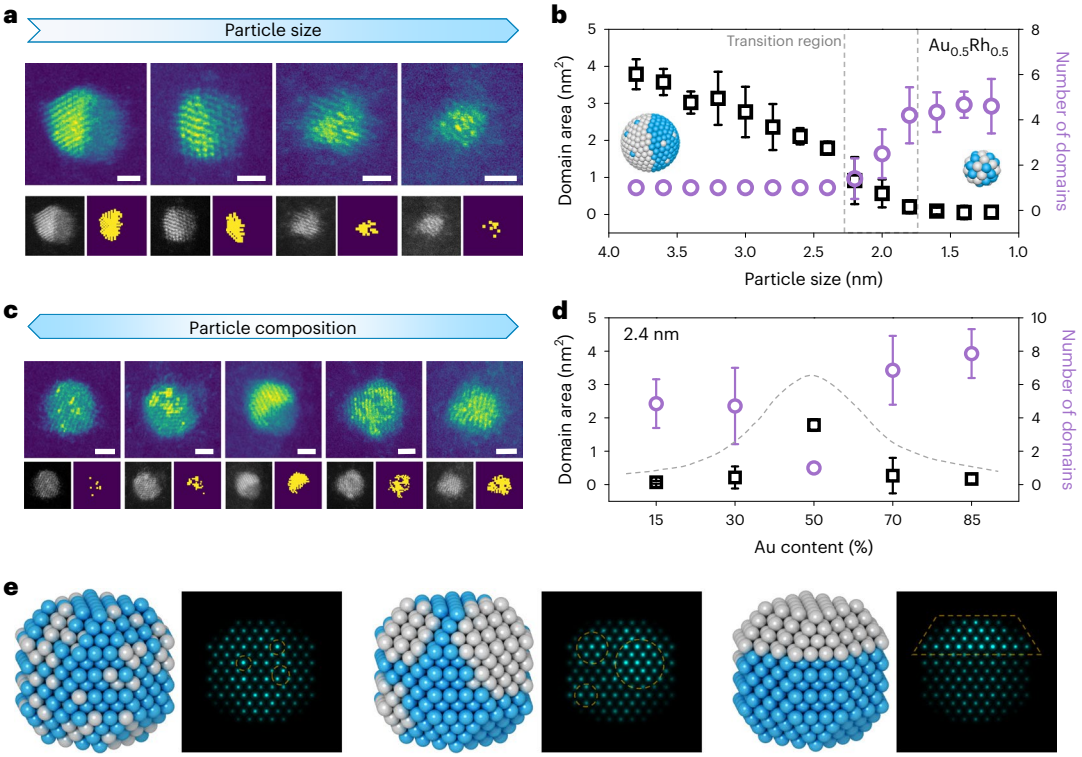

Fig. 3 | Effect of particle size and composition on the phase separation behaviour between Au and Rh. a, Size-dependent phase separation in $Au_{0.5}Rh_{0.5}$ nanoparticles of size from 4 to 1 nm. Scale bars, 1 nm. The bottom row shows the HAADF-STEM images of the nanoparticles and corresponding image analysis showing the Au domains in the particles. The top row shows the HAADF-STEM images with the Au domains highlighted. **b**, Dependence of the number and cross-sectional area of Au domains in $Au_{0.5}Rh_{0.5}$ nanoparticles on the nanoparticle size. The dashed rectangle outlines the transition region. For each data point, the sample size is 20 particles. The data are presented as mean values ± standard deviation. **c**, Composition-dependent phase separation of Au and Rh in nanoparticles of size about 3 nm. Scale bars, 1 nm. From left to right, the particle compositions are $Au_{0.15}Rh_{0.85}$, $Au_{0.3}Rh_{0.7}$, $Au_{0.5}Rh_{0.5}$, $Au_{0.7}Rh_{0.3}$ and $Au_{0.85}Rh_{0.15}$. **d**, Dependence of the number and cross-sectional area of the minor element's domains on the particle composition at a fixed particle size. The dashed lines depict the change in domain area as guides for the eye. For each data point, the sample size is 20 particles. The data are presented as mean values ± standard deviation. **e**, Simulated HAADF-STEM images and corresponding models of $Au_{0.3}Rh_{0.7}$ particles with an alloyed, intermediate or heterostructured state. Grey, Au atoms; blue, Rh atoms. The orange circles and trapezoid highlight the distribution of Au atoms in the nanoparticles.

that is, the Au domains in a Rh-rich nanoparticle and Rh domains in a Au-rich nanoparticle (Fig. 3 and Supplementary Figs. 13–21). An algorithm based on a random walk model was developed to detect the bright Au domains in the STEM images (Supplementary Fig. 13). The information of Rh domains can be extracted by subtracting the Au domains from the nanoparticle (Supplementary Fig. 14). In particular, for alloyed $Au_{0.15}Rh_{0.85}$ and $Au_{0.85}Rh_{0.15}$ (Fig. 3 and Supplementary Fig. 15d,e), the cross-sectional area of the minor element's domains is between 0.05 and 0.20 nm^2, suggesting that their cross-sectional area is about 1–4 atoms in an alloyed nanoparticle. In this work, we use 0.2 nm^2 as the critical cross-sectional area of domains to differentiate the alloyed and separated states of Au–Rh. For nanoparticles within the compositional range of 30–70% Au (Supplementary Fig. 15a–c), a transition region can be identified for each different composition. In these regions, the nanoparticles start to adopt an intermediate structure that is neither heterostructured nor alloyed. Taking $Au_{0.5}Rh_{0.5}$ as an example (Fig. 3a,b), the number of Au domains in a nanoparticle persists at one and the Au domain area gradually decreases when the particle size is decreased from 4.0 to 2.2 nm, because $Au_{0.5}Rh_{0.5}$ has a heterodimer structure in this region. When the particle size falls in the range of 2.2–1.8 nm, the transition region for $Au_{0.5}Rh_{0.5}$, Au splits into several domains in a nanoparticle due to enhanced Au–Rh mixing. Consequently, the number of Au domains increases from 1 to around 5 until a plateau is reached, and the cross-sectional area of Au domains decreases from 0.9 to ~0.2 nm^2, approaching the borderline of Au–Rh alloy. The Au domain area remains <0.2 nm^2 in sub-1.8 nm $Au_{0.5}Rh_{0.5}$ nanoparticles due to the alloying of Au and Rh. The quantitative analysis corroborates that $Au_{0.5}Rh_{0.5}$ experiences a phase-separation-to-alloy transition when particle size decreases, with the intermediate state occurring between 2.2 and 1.8 nm. For $Au_{0.3}Rh_{0.7}$ and $Au_{0.7}Rh_{0.3}$ nanoparticles (Supplementary Fig. 15a,c), a similar trend can be observed. The transition regions for $Au_{0.3}Rh_{0.7}$ and $Au_{0.7}Rh_{0.3}$ are 3.2–2.0 nm and 3.7–2.2 nm, respectively. The inverse miscibility relationship of Au–Rh in the $Au_{0.3}Rh_{0.7}$, $Au_{0.5}Rh_{0.5}$ and $Au_{0.7}Rh_{0.3}$ nanoparticles supports the conclusion that small material size can flip over the thermodynamic phase separation behaviour of immiscible elements.

The phase-separation-to-alloy transition is also impacted by particle composition. In general, Au–Rh is more resistant to this transition when the particle contains a closer content of Au and Rh (Fig. 3c–e and Supplementary Fig. 16). Figure 3c shows a parallel comparison between the five compositions at a fixed particle size of ~3 nm. $Au_{0.5}Rh_{0.5}$ exhibits a heterodimer structure because the highest repulsion energy between Au–Rh in this composition (Supplementary Fig. 22) can overcome the size-induced mixing effect and lead to the phase-separated structure (Fig. 3c, third column). The mixing enthalpy of $Au_{0.3}Rh_{0.7}$ and $Au_{0.7}Rh_{0.3}$ is reduced by 16% over that of $Au_{0.5}Rh_{0.5}$ (Supplementary Fig. 22a). For these two compositions, both interaction between Au and Rh and the surface effect are at work to dictate the phase separation state. The nanosize effect increases the mixing capability between Au and Rh, whereas the moderate repulsion energy between them prevents their full alloying. Consequently, Au and Rh split into several domains (>0.2 nm^2) in $Au_{0.3}Rh_{0.7}$ and $Au_{0.7}Rh_{0.3}$ nanoparticles, respectively

https://doi.org/10.1038/s41565-024-01626-0

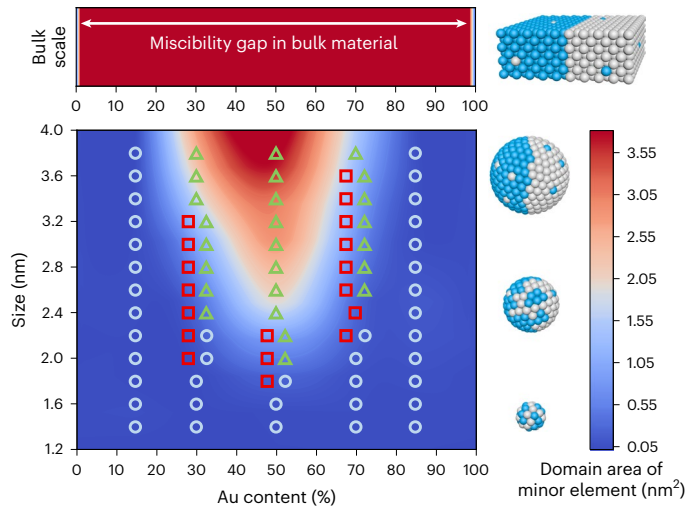

Fig. 4 | Experimental Au–Rh phase diagram at the nano- and cluster length scales and its comparison with the bulk miscibility gap between Au–Rh. The phase map is projected based on the quantitative analysis of the cross-section area of the minor element domains, that is, Au domains in Rh-rich nanoparticles ($Au_{0.15}Rh_{0.85}$, $Au_{0.3}Rh_{0.7}$ and $Au_{0.5}Rh_{0.5}$) and Rh domains in Au-rich nanoparticles ($Au_{0.7}Rh_{0.3}$ and $Au_{0.85}Rh_{0.15}$). The experimentally observed data points of alloyed (circles, light blue), intermediate (squares, red) and heterostructured (triangles, green) nanoparticles are shown on the map. The schematic depicts the transition from phase separation to alloying in Au–Rh nanoparticles.

(Fig. 3c, second and fourth columns). For $Au_{0.15}Rh_{0.85}$ and $Au_{0.85}Rh_{0.15}$, the repulsion energy is reduced by 49% over that of $Au_{0.5}Rh_{0.5}$ (Supplementary Fig. 22a), resulting in a smaller obstacle for Au and Rh to mix. Quantitative analysis confirms that these two compositions prefer an alloyed structure, where Au or Rh form domains smaller than 0.2 nm^2 in the nanoparticles (Fig. 3c, first and fifth columns).

To combine all of our quantitative analysis, we plotted a size-dependent phase diagram of Au–Rh (Fig. 4). The experimental data points of heterostructured, intermediate and alloyed particles are denoted by green Δ, red □ and blue ○, respectively. Compared with the large miscibility gap in the Au–Rh bulk phase diagram, the gap is diminished in sub-4 nm Au–Rh particles and can be closed across the entire compositional range in the sub-2 nm size regime. With the decrease in particle size, Au–Rh nanoparticles exhibit a transition from heterostructured to intermediate and alloyed, whereas the actual transition occurs in a different size region for different compositions. The closer the Au/Rh ratio is to an equimolar value, the smaller is the particle size needed to initiate this transition. The major factor that causes the thermodynamic behaviour change can be attributed to the increased surface effect. When one considers nanoparticles in the sub-4 nm size regime, the fraction of surface atoms is exponentially increased to a considerable level (Supplementary Fig. 23), making them non-negligible from the thermodynamic perspective.

Theoretical analysis of the nanoscale phase separation behaviour

Semi-empirical models have been widely used to explain the nanosize effect on the mixing pattern of immiscible elements[39–41]. For nanoparticles, the undercoordinated atoms on the surface are considered to diminish the interaction between incompatible atoms like Au and Rh, which facilitates the alloying of elements. In comparison, computational simulations based on density functional theory (DFT) or molecular dynamics have predicted core–shell Au–Rh nanoparticles as the stable structure[21,46,47]. However, these models neglect surface passivation effects such as the adsorption of environmental species, which probably react with the nanoparticle surface area during synthesis.

Given the different structures reported in the literature, we developed models that treat different types of Au–Rh structure (heterodimer, alloy and core–shell structures) to interpret how particle size, composition and available adsorbates affect miscibility (Supplementary Fig. 24). DFT was used to calculate the surface energy of Au and Rh, the interfacial energy between Au and Rh, the interaction parameter of Au–Rh at different compositions (Supplementary Fig. 25) and the surface adsorption energy of various species such as CH_3 (Supplementary Table 1). The models were parametrized with the DFT calculations to calculate the total energy of Au–Rh nanoparticles and assess the thermodynamically stable configurations (see the discussion following Supplementary Fig. 24). The result confirms the size-dependent stability of each configuration in the Au–Rh nanoparticle system in agreement with the particles synthesized here (Fig. 5). A smaller particle size leads to an enhanced surface effect that suppresses the mixing enthalpy towards a more negative value and promotes alloying, whereas an equimolar elemental ratio results in a maximized repulsion energy between Au–Rh and facilitates phase separation. The alloying is also promoted by configurational entropy. However, the entropy change from separated to alloyed states is relatively small compared with the variation in enthalpy from bulk Au–Rh to ultrasmall particles (Supplementary Fig. 22), rendering entropy to be a minor factor in determining the mixing state. Although the model confirms previous computational studies of Au–Rh nanoparticles in a vacuum, which identify the core–shell configuration as the most stable structure[21,46,47], we also find that core–shell nanoparticles are not expected to be stable when surface passivation from environmental species are considered (Fig. 5 and Supplementary Figs. 22 and 24–28).

In a vacuum environment, the surface energy difference for Au and Rh is calculated to be −9.8 eV nm^{-2}. With this value, the model predicts that Au–Rh particles would strongly favour the core–shell character with Au enriched on the surface (Fig. 5a). However, during synthesis, organic species may adsorb to the undercoordinated surface atoms, and probably remain even though the nanoparticles are plasma-cleaned in O_2 and re-annealed in H_2. Although the bare surface energy of Au is lower than that of Rh, adsorbates tend to bind more strongly to Rh than Au surfaces (Supplementary Table 1). Therefore, surface passivation has the effect of reducing the difference in surface energies of each element, thereby destabilizing the core–shell phase and inducing a phase transformation from the core–shell to heterodimer or alloy geometry (Fig. 5 and Supplementary Figs. 26 and 27). According to a screening of several possible adsorbates, there are several organic adsorbates that bind strongly enough to each surface to induce this transformation (Supplementary Table 1 and Supplementary Fig. 27). The predicted equilibrium structure of passivated ultrasmall Au–Rh nanoparticles at 500 °C is presented in Fig. 5b, which is in good agreement with the experimental findings. Together, our experimental study combined with the theoretical analysis show that the thermodynamic phase stability of immiscible elements can change owing to the size-dependent surface-environment-induced effects.

Conclusions

We have systematically explored the phase separation of Au and Rh in a nanoparticle. Despite the high incompatibility between Au and Rh in a bulk material, miniaturizing Au–Rh materials to the nano- and cluster size regime can switch their miscibility relationship from immiscible to fully alloyable, as we have demonstrated for sub-2 nm Au–Rh alloy nanoparticles across a broad compositional range. We have found that the change in mixing behaviour is affected by particle size, composition and surface passivation. Surface passivation reduces the relative energy of Rh with respect to Au, destabilizing the core–shell geometries and instead favouring the heterodimer and alloy phases. In passivating environments, a thermodynamic model parametrized by DFT calculations validates that Au and Rh will alloy at ultrasmall sizes. Our work quantitatively proves that the bulk phase diagram does not

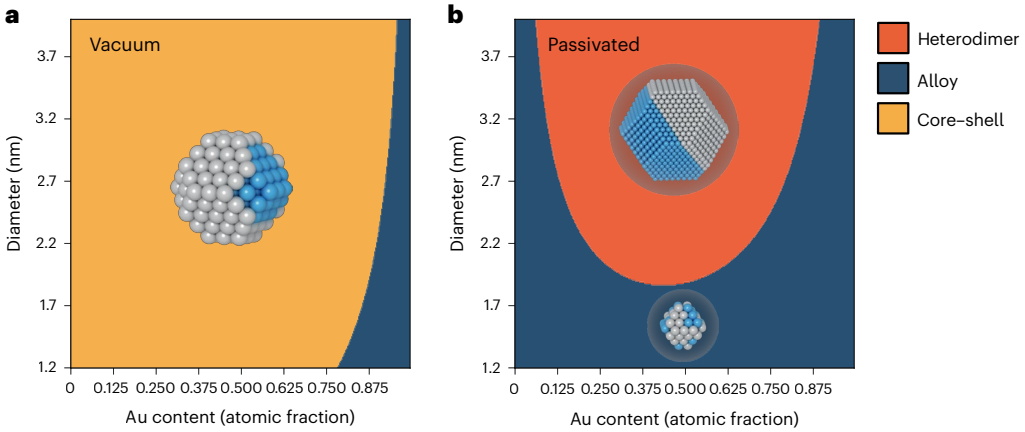

Fig. 5 | Theoretical phase diagrams of the thermodynamic configurations of Au–Rh nanoparticles. a, Size-dependent phase diagram expected for Au–Rh particles in ultrahigh-vacuum environments. Yellow phase, core–shell; dark-blue phase, alloy. **b**, Size-dependent phase diagram expected with passivated surfaces of Au–Rh. Red phase, heterostructure; dark-blue phase, alloy. Each diagram is for particles at 500 °C. Supplementary Figs. 27 and 28 show the phase diagrams for the system with different passivation strengths and at variable temperatures. The inset shows models of core–shell, heterodimer and alloy configurations; the grey atoms are Au and the blue atoms are Rh. The theoretical phase diagram with passivated surfaces matches well with the diagram in Fig. 4.

necessarily apply to nanoscale materials. The experimental results call for the exploration of the phase separation behaviour of multielement nanosystems, before conclusively interpreting their thermodynamic structure. Understanding the thermodynamic behaviour of multielement nanoparticles will open up the ability to engineer the structures and properties of multielement nanoparticles for real-life applications.

Online content

Any methods, additional references, Nature Portfolio reporting summaries, source data, extended data, supplementary information, acknowledgements, peer review information; details of author contributions and competing interests; and statements of data and code availability are available at https://doi.org/10.1038/s41565-024-01626-0.

References

1. Xie, C. L. et al. Tandem catalysis for CO_2 hydrogenation to C_2-C_4 hydrocarbons. *Nano Lett.* **17**, 3798–3802 (2017).
2. Lewis, R. J. et al. Highly efficient catalytic production of oximes from ketones using in situ-generated H_2O_2. *Science* **376**, 615–620 (2022).
3. Yang, T. et al. Ultrahigh-strength and ductile superlattice alloys with nanoscale disordered interfaces. *Science* **369**, 427–432 (2020).
4. Shi, P. J. et al. Hierarchical crack buffering triples ductility in eutectic herringbone high-entropy alloys. *Science* **373**, 912–918 (2021).
5. He, Q. F. et al. A highly distorted ultraelastic chemically complex Elinvar alloy. *Nature* **602**, 251–257 (2022).
6. Oh, N. R. et al. Double-heterojunction nanorod light-responsive LEDs for display applications. *Science* **355**, 616–619 (2017).
7. Ibrar, M. & Skrabalak, S. E. Designer plasmonic nanostructures for unclonable anticounterfeit tags. *Small Struct.* **2**, 2100043 (2021).
8. Jiang, B. B. et al. High-entropy-stabilized chalcogenides with high thermoelectric performance. *Science* **371**, 830–834 (2021).
9. Jiang, B. B. et al. High figure-of-merit and power generation in high-entropy GeTe-based thermoelectrics. *Science* **377**, 208–213 (2022).
10. Pendharkar, M. et al. Parity-preserving and magnetic field-resilient superconductivity in InSb nanowires with Sn shells. *Science* **372**, 508–511 (2021).
11. Okamoto, H., Schlesinger, M. E. & Mueller, E. M. (eds) *Binary Alloy Phase Diagrams* (ASM International, 2016).
12. Loffler, T. et al. Discovery of a multinary noble metal-free oxygen reduction catalyst. *Adv. Energy Mater.* **8**, 1802269 (2018).
13. Kusada, K. et al. Nonequilibrium flow-synthesis of solid-solution alloy nanoparticles: from immiscible binary to high-entropy alloys. *J. Phys. Chem. C* **125**, 458–463 (2021).
14. Chen, Y. F. et al. Synthesis of monodisperse high entropy alloy nanocatalysts from core@shell nanoparticles. *Nanoscale Horiz.* **6**, 231–237 (2021).
15. Wang, C. Y. et al. Facet-dependent deposition of highly strained alloyed shells on intermetallic nanoparticles for enhanced electrocatalysis. *Nano Lett.* **17**, 5526–5532 (2017).
16. Chen, P. C. et al. Polyelemental nanoparticle libraries. *Science* **352**, 1565–1569 (2016).
17. Chen, P. C. et al. Interface and heterostructure design in polyelemental nanoparticles. *Science* **363**, 959–964 (2019).
18. Chen, P. C. et al. Chain-end functionalized polymers for the controlled synthesis of sub-2 nm particles. *J. Am. Chem. Soc.* **142**, 7350–7355 (2020).
19. Fenton, J. L., Steimle, B. C. & Schaak, R. E. Tunable intraparticle frameworks for creating complex heterostructured nanoparticle libraries. *Science* **360**, 513–517 (2018).
20. Steimle, B. C., Fenton, J. L. & Schaak, R. E. Rational construction of a scalable heterostructured nanorod megalibrary. *Science* **367**, 418–424 (2020).
21. Piccolo, L. et al. Understanding and controlling the structure and segregation behaviour of AuRh nanocatalysts. *Sci. Rep.* **6**, 35226 (2016).
22. Chen, P.-C. et al. Chemical and structural evolution of AgCu catalysts in electrochemical CO_2 reduction. *J. Am. Chem. Soc.* **145**, 10116–10125 (2023).
23. Wang, B. et al. General synthesis of high-entropy alloy and ceramic nanoparticles in nanoseconds. *Nat. Synth.* **1**, 138–146 (2022).
24. Yang, C. L. et al. Sulfur-anchoring synthesis of platinum intermetallic nanoparticle catalysts for fuel cells. *Science* **374**, 459–464 (2021).
25. Feng, G. et al. Sub-2 nm ultrasmall high-entropy alloy nanoparticles for extremely superior electrocatalytic hydrogen evolution. *J. Am. Chem. Soc.* **143**, 17117–17127 (2021).
26. Buendia, F., Vargas, J. A., Johnston, R. L. & Beltran, M. R. Study of the stability of small AuRh clusters found by a genetic algorithm methodology. *Comput. Theor. Chem.* **1119**, 51–58 (2017).

27. Rahm, J. M. & Erhart, P. Understanding chemical ordering in bimetallic nanoparticles from atomic-scale simulations: the competition between bulk, surface, and strain. *J. Phys. Chem. C* **122**, 28439–28445 (2018).
28. Christensen, A., Stoltze, P. & Norskov, J. K. Size dependence of phase-separation in small bimetallic clusters. *J. Phys. Condens. Matter* **7**, 1047–1057 (1995).
29. Fevre, M., Le Bouar, Y. & Finel, A. Thermodynamics of phase-separating nanoalloys: single particles and particle assemblies. *Phys. Rev. B* **97**, 195404 (2018).
30. Srivastava, C., Chithra, S., Malviya, K. D., Sinha, S. K. & Chattopadhyay, K. Size dependent microstructure for Ag-Ni nanoparticles. *Acta Mater.* **59**, 6501–6509 (2011).
31. Kusada, K., Yamauchi, M., Kobayashi, H., Kitagawa, H. & Kubota, Y. Hydrogen-storage properties of solid-solution alloys of immiscible neighboring elements with Pd. *J. Am. Chem. Soc.* **132**, 15896–15898 (2010).
32. Zhang, Q. et al. Selective control of fcc and hcp crystal structures in Au-Ru solid-solution alloy nanoparticles. *Nat. Commun.* **9**, 510 (2018).
33. Zhang, H., Wang, L., Lu, L. & Toshima, N. Preparation and catalytic activity for aerobic glucose oxidation of crown jewel structured Pt/Au bimetallic nanoclusters. *Sci. Rep.* **6**, 30752 (2016).
34. Toshima, N. & Hirakawa, K. Polymer-protected bimetallic nanocluster catalysts having core/shell structure for accelerated electron transfer in visible-light-induced hydrogen generation. *Polym. J.* **31**, 1127–1132 (1999).
35. Toshima, N. & Yonezawa, T. Bimetallic nanoparticles-novel materials for chemical and physical applications. *New J. Chem.* **22**, 1179–1201 (1998).
36. Meischein, M. et al. Elemental (im-)miscibility determines phase formation of multinary nanoparticles co-sputtered in ionic liquids. *Nanoscale Adv.* **4**, 3855–3869 (2022).
37. Rajeeva, B. B. et al. Accumulation-driven unified spatiotemporal synthesis and structuring of immiscible metallic nanoalloys. *Matter* **1**, 1606–1617 (2019).
38. Feng, J. C. et al. Unconventional alloys confined in nanoparticles: building blocks for new matter. *Matter* **3**, 1646–1663 (2020).
39. Qi, W. H. & Wang, M. P. Size effect on the cohesive energy of nanoparticle. *J. Mater. Sci. Lett.* **21**, 1743–1745 (2002).
40. Xiong, S. Y., Qi, W. H., Huang, B. Y. & Wang, M. P. Size-, shape- and composition-dependent alloying ability of bimetallic nanoparticles. *ChemPhysChem* **12**, 1317–1324 (2011).
41. Qi, W. H., Huang, B. Y. & Wang, M. P. Size and shape-dependent formation enthalpy of binary alloy nanoparticles. *Phys. B* **404**, 1761–1765 (2009).
42. Sneed, B. T., Young, A. P. & Tsung, C. K. Building up strain in colloidal metal nanoparticle catalysts. *Nanoscale* **7**, 12248–12265 (2015).
43. Ferrando, R. *Structure and Properties of Nanoalloys* (Elsevier, 2016).
44. Chen, P. C. et al. Revealing the phase separation behavior of thermodynamically immiscible elements in a nanoparticle. *Nano Lett.* **21**, 6684–6689 (2021).
45. Sohlberg, K., Pennycook, T. J., Zhou, W. & Pennycook, S. J. Insights into the physical chemistry of materials from advances in HAADF-STEM. *Phys. Chem. Chem. Phys.* **17**, 3982–4006 (2015).
46. Vanzan, M., Jones, R. M., Corni, S., D'Agosta, R. & Baletto, F. Exploring AuRh nanoalloys: a computational perspective on the formation and physical properties. *ChemPhysChem* **23**, e202200035 (2022).
47. Valizadeh, Z. & Abbaspour, M. Surface energy, relative stability, and structural properties of Au-Pt, Au-Rh, Au-Cu, and Au-Pd nanoclusters created in inert-gas condensation process using MD simulation. *J. Phys. Chem. Solids* **144**, 109480 (2020).

Methods

Materials

Gold(III) chloride and rhodium(III) nitrate hydrate were purchased from Sigma-Aldrich and used without further purification. Polystyrene-*b*-poly(2-vinylpyridine) (M_n = 34-*b*-18 kg mol^{-1}; dispersity, 1.11) was purchased from Polymer Source and used as received. Anhydrous toluene and methanol were purchased from Sigma-Aldrich and used as received. Nickel and gold TEM grids with a 3 nm ultrathin carbon film coated on a lacey carbon support were purchased from Ted Pella.

Synthesis of Au–Rh nanoparticles in micelle reactors

Polymer micelles were prepared by dissolving 5 mg of polystyrene-*b*-poly(2-vinylpyridine) in 1 ml of toluene. $AuCl_3$ was first dissolved in 10 µl of methanol and then added to the micelle solution. The mixture solution was successively sonicated using a tip sonicator (SONICS VCX 500, 2 mm tip) at a 20% amplitude for 60 s and at a 40% amplitude for 60 s to facilitate the dispersion of $AuCl_3$ in the micelles. After that, the micelle solution was stirred at room temperature for 6 h. $Rh(NO_3)_3$ was dissolved in 10 µl methanol and added to the micelle solution to get a desired molar ratio between $AuCl_3$ and $Rh(NO_3)_3$. The resulting mixture solution was further stirred at room temperature for 12 h before use. For the synthesis of $Au_{0.15}Rh_{0.85}$, $Au_{0.3}Rh_{0.7}$, $Au_{0.5}Rh_{0.5}$, $Au_{0.7}Rh_{0.3}$ and $Au_{0.85}Rh_{0.15}$ nanoparticles, the molar ratios between Au and Rh salts were set to 1:1, 2:1, 3:1, 5:1 and 8:1, respectively. The molar ratio between the pyridyl groups and total metal precursors was controlled between 32:1 to 128:1 to obtain nanoparticles of size from 4 to 1 nm. To convert micelles into nanoparticles, the solution of precursor-loaded micelles was first spin coated on a TEM grid at a spin rate of 4,000 r.p.m. The TEM grid was treated with O_2 plasma (Harrick Plasma Cleaner, PDC-32G) for 7 min, followed by thermal annealing under flowing Ar/H_2 (90/10, v/v) in a tube furnace. The annealing conditions were designed as follows: ramp to 150 °C in 1 h, hold at 150 °C for 4 h, ramp to 250 °C in 1 h, hold at 250 °C for 4 h, ramp to 400 °C in 1 h, hold at 400 °C for 1 h, ramp to 500 °C in 1 h, hold the grids at 500 °C for 12 h and finally cool down to room temperature in 5 h. The stepwise annealing between 150 and 400 °C can facilitate the nucleation, growth and coarsening of the metal species in each micelle reactor to form a single nanoparticle. The last annealing step at 500 °C decomposes the micelles and ensures that Au–Rh reaches a thermodynamic equilibrium. Plasma cleaning (Fischione Plasma Cleaner, Model 1020) under Ar/O_2 (75/25, v/v) was applied on the TEM grids for 10 s to remove the carbon residues formed on the synthesized nanoparticles. The TEM grids were then annealed at 500 °C under flowing Ar/H_2 (90/10, v/v) for another 12 h and cooled down to room temperature within 12 h before characterization.

Characterization

A Hitachi 7650 TEM instrument operated at 100 kV was used to record low-resolution TEM images of the polymer micelles and nanoparticles. EDS and STEM characterizations of the nanoparticles were performed on a Thermo Fisher Scientific Titan 60–300 TEM instrument at an acceleration voltage of 300 kV. The electron microscope is equipped with four silicon drift EDS detectors with a total solid angle of 0.7 steradians. The Lα peaks of Au and Rh in the EDS spectra were used for elemental mapping and composition quantification of the nanoparticles. The atomic compositions were calculated using the standardless Cliff–Lorimer correction method. Each EDS map was built based on the accumulation of 150 frames with a pixel dwell time of 8 µs. Bruker ESPRIT v.1.9 software was used for background subtraction in the EDS maps. Electron energy loss spectroscopy maps of the nanoparticles were acquired on a fifth-order aberration-corrected STEM instrument (Cornell Nion UltraSTEM) operated at 100 keV with a beam convergence semi-angle of 30 mrad. Electron energy loss spectroscopy images were acquired with a 0.25 eV per channel energy dispersion (energy resolution, 1.0 eV) in a Gatan spectrometer with a size of 100 × 100 pixels and an acquisition time of 10 ms per pixel. The Rh and Au elemental maps were extracted using their $M_{5,4}$ edges from the electron energy loss spectroscopy images and processed using principal component analysis (three components) and the linear combination of power law in ImageJ v.1.52 software to subtract the background. Atomic-resolution HAADF-STEM characterization of the nanoparticles were conducted on TEAM0.5, an aberration-corrected Thermo Fisher Scientific Titan 80–300 TEM instrument, at an acceleration voltage of 200 kV. Typical aberration coefficients used for imaging are C1 = −2.15 nm, A1 = 1.68 nm, A2 = 14.50 nm, B2 = 14.90 nm, C3 = −228.00 nm, A3 = 120.00 nm, S3 = 199.00 nm, A4 = 4.19 µm, D4 = 3.03 µm, B4 = 4.28 µm, C5 = −90.58 µm, A5 = 118.00 µm. The HAADF-STEM images were acquired using a high-angle annular dark-field detector with collection semi-angles from 58 to 265 mrad and a probe convergence semi-angle of 30 mrad. The probe size is ~0.5 Å. The beam current was set to 70 pA for the imaging of 2–4 nm nanoparticles and was set to ~6 pA for the imaging of 1–2 nm nanoparticles. All the HAADF-STEM images were recorded in a 1,024 × 1,024 pixel^2 format at a pixel dwell time of 3 µs. The electron dose rate was about 780 e^- Å^{-2} s^{-1}. A short-pass filter was applied in the Fourier space for the images of sub-2 nm Au–Rh particles to improve the image quality. A typical filter threshold is 1/1.5 or 1 Å^{-1}, corresponding to 1.5 or 1.0 Å. The STEM image simulation of single Au and Rh atoms was performed using the QSTEM v.2.50 software[48]. The experimental microscope parameters described above were used as parameters for the image simulation.

Quantitative analysis of HAADF-STEM images

An algorithm based on a random walk model was developed to detect the bright Au domains in the STEM images. The algorithm first automatically detects a nanoparticle from the full frame of a STEM image and crops the nanoparticle out for analysis. A threshold value that is the average intensity of the bright and dark domains in the STEM images is selected to distinguish Au-rich and Rh-rich domains. A brush size that approximately equals to the size of the atom and a step size that is equal to the size of the brush are selected. The following random walk model is then used to identify all the bright domains that correspond to Au. (1) In a typical round of random walk analysis, the algorithm first identifies the brightest pixel in the image and uses it as a probing pixel. (2) Around the probing pixel, it calculates the pixel intensities of eight patches (of the size of the brush) with a step size away from the probing pixel. If any patch has an intensity above the threshold value, it identifies that patch to be a propagation candidate, which will be selected as the new probing pixel in the next propagation step. (3) After each step, a group of propagation candidates will be used as the new probing pixels to start the next propagation step. (4) We set the number of patches around every probing pixel in each propagation step to be eight, which proves to be sufficient to cover a continuous domain. (5) The propagation of probing pixels ends when the algorithm cannot find any connected patch with intensity above the threshold value. Then, the enclosed map of the propagation trajectory is recognized as a domain. (6) After one round of random walk analysis, the recognized bright domains will be excluded from the image; therefore, those pixels will not be recognized as a propagation candidate in the future analysis. (7) The next round of random walk analysis then starts to look for another brightest pixel that is outside of the domain identified before, and this pixel will be the starting pixel for a new domain. (8) We repeat the domain search for 50 times. In principle, all the bright domains within a nanoparticle can be recognized. After all the random walk analyses, any pixel within a particle identified as a part of a domain will be marked by intensity 1 and the other pixels will be given an intensity of 0. We binarize the image and the number of domains is analysed by a function in the MATLAB v.R2021b image processing toolbox, namely, bwconncomp(), which finds and counts the connected components in the binary image. The size and amount of Au domains in a nanoparticle image can then be calculated (Supplementary Fig. 13). The information of Rh domains can also be extracted by subtracting the Au domains from the entire nanoparticle (Supplementary Fig. 14).

DFT calculations and theoretical analysis

All the DFT calculations were performed with the Vienna ab initio simulation package 6 (ref. 49), with the generalized gradient approximation and the Perdew–Burke–Ernzerhof exchange–correlation functional, the projector augmented wave method[50,51] and spin polarization. All the calculations of bulk phases were performed with a Brillouin-zone sampling of 10 × 10 × 10. Slab and interface calculations were performed with a Brillouin-zone sampling of 4 × 4 × 1, with the longest cell dimension having a sampling of 1. To avoid spurious interactions in the periodic boundary conditions, all the distances between non-interacting surfaces were set to be greater than 10 Å with vacuum separation. The DFT-calculated values of the Au–Rh system, including surface energy, interfacial energy and interaction parameters, were used to evaluate the total energy of the nanoparticles of different sizes, compositions and configurations.

Data availability

The data supporting the findings of this study are available within the Article and its Supplementary Information, and are available from the corresponding author on reasonable request.

Code availability

The source codes of the algorithm for the HAADF-STEM image analysis are available via Zenodo at https://doi.org/10.5281/zenodo.10510952.

References

48. Koch, C. T. *Determination of Core Structure Periodicity and Point Defect Density along Dislocations*. PhD thesis, Arizona State Univ. (2002).
49. Kresse, G. & Furthmuller, J. Efficient iterative schemes for ab initio total-energy calculations using a plane-wave basis set. *Phys. Rev. B* **54**, 11169–11186 (1996).
50. Kresse, G. & Joubert, D. From ultrasoft pseudopotentials to the projector augmented-wave method. *Phys. Rev. B* **59**, 1758–1775 (1999).
51. Perdew, J. P., Burke, K. & Ernzerhof, M. Generalized gradient approximation made simple. *Phys. Rev. Lett.* **77**, 3865–3868 (1996).

Acknowledgements

This work was supported by Director, Office of Science, Office of Basic Energy Sciences, Chemical Sciences, Geosciences & Biosciences Division, US Department of Energy (DOE), under Contract DE-AC02-05CH11231, FWP CH030201 (Catalysis Research Program). Work at the Molecular Foundry was supported by the Office of Science, Office of Basic Energy Sciences, US DOE, under contract no. DE-AC02-05CH11231. This work made use of the TEM facilities at the Cornell Center for Materials Research (CCMR), which are supported through the National Science Foundation Materials Research Science and Engineering Center (NSF MRSEC) program (DMR-1719875). P.-C.C. acknowledges support from Kavli ENSI Heising-Simons Fellowship. J.J. acknowledges fellowship support from Suzhou Industrial Park. Y.Y. acknowledges support from Miller Fellowship. C.A.M. acknowledges the National Defense Science and Engineering Graduate (NDSEG) fellowship and the Kavli ENSI Graduate Student Fellowship for financial support. This research used resources of the National Energy Research Scientific Computing Center, a US DOE Office of Science User Facility supported by the Office of Science of the US DOE under contract no. DE-AC02-05CH11231 using NERSC award BES-ERCAP0024004.

Author contributions

P.-C.C. and P.Y. conceived the ideas and designed the experiments. P.-C.C. performed the nanoparticle synthesis and conducted the electron microscopy characterization. M.G. designed the quantitative analysis algorithm. P.-C.C. and M.G. analysed the electron microscopy characterization data and performed the STEM image simulation. C.A.M. and K.A.P. performed the DFT calculations and theoretical analysis. C.S., J.J., Y.Y. and A.L.M. discussed the experimental results. P.-C.C., M.G. and P.Y. wrote the manuscript with editorial input from the other authors. P.Y. supervised the project.

Competing interests

The authors declare no competing interests.

Additional information

Supplementary information The online version contains supplementary material available at https://doi.org/10.1038/s41565-024-01626-0.

Correspondence and requests for materials should be addressed to Peidong Yang.

Peer review information *Nature Nanotechnology* thanks Hiroshi Kitagawa and the other, anonymous, reviewer(s) for their contribution to the peer review of this work.